HCIT Contrast Performance Sensitivity Studies: Simulation versus Experiment

***Erkin Sidick, Stuart Shaklan, John Krist, Eric J. Cady, Brian Kern, and Kunjithapatham Balasubramanian**
Jet Propulsion Laboratory, California Institute of Technology, 4800 Oak Grove Drive, Pasadena, CA 91109, USA

ABSTRACT

Using NASA's High Contrast Imaging Testbed (HCIT) at the Jet Propulsion Laboratory, we have experimentally investigated the sensitivity of dark hole contrast in a Lyot coronagraph for the following factors: 1) Lateral and longitudinal translation of an occulting mask; 2) An opaque spot on the occulting mask; 3) Sizes of the controlled dark hole area. Also, we compared the measured results with simulations obtained using both MACOS (Modeling and Analysis for Controlled Optical Systems) and PROPER optical analysis programs with full three-dimensional near-field diffraction analysis to model HCIT's optical train and coronagraph.

Key words: Coronagraphy, adaptive optics, space telescopes, exoplanets

1. INTRODUCTION

This paper presents both simulated and measured results on the sensitivity of broadband contrast of a Lyot coronagraph on the High-Contrast Imaging Testbed (HCIT) at NASA's Jet Propulsion Laboratory (JPL). This testbed is the Exoplanet Exploration Program's primary platform for experimentation [1-3]. It is used to provide laboratory validation of key technologies as well as demonstration of a flight-traceable approach to implementation. It employs a 48x48 actuators deformable-mirror (DM) and a broadband wavefront correction algorithm called Electric Field Conjugation (EFC) to obtain the required 10^{-10} contrast [4]. We have investigated the effects of the following factors on the system performance and the efficiency of the EFC algorithm: Lateral and longitudinal translation of the occulter, an opaque spot on the occulter, and the size of the controlled dark-hole area. The laboratory testing was carried out with either a 2%-narrowband or a 10%-broadband light. The simulations were conducted with both MACOS (Modeling and Analysis for Controlled Optical Systems) [5] and PROPER [6], and their results were compared with measurements. We got fairly good agreement between the measurement and the simulation. In an earlier paper we reported on model sensitivities for the number and position of dead actuators, and beam walk due to translation of a flat optic in the beam [7].

2. BACKGROUND

2.1 The HCIT Optical System

The schematic diagram of the HCIT layout in the *xz*-plane is shown in Figure 1. Artificial starlight is created by a 5μm pinhole illuminated by an optical fiber. We use a broadband light source centered at wavelength λ=800nm in combination with five 2%-bandpass filters whose passbands are centered at 768, 784, 800, 816 and 832nm, respectively. For some experiments only the 768, 800 and 832nm filters were employed. An off-axis parabolic mirror (OAP1) collimates the light from the pinhole and directs it to a high-density, 64x64 actuator DM, which performs wavefront control. A circular aperture mask on the DM defines the system pupil of the HCIT, and can have a diameter of up to *D*=64mm. However, the current HCIT was implemented with *D*=48mm inscribed in an area covered by 48x48 actuators, and we use this same *D* value in the simulations of this paper. After the DM, the collimated light is imaged onto the focal plane of the occulting mask by OAP2 and a flat-mirror (FM). The occulting mask attenuates the starlight, and has little effect on the light of a planet if present. The "back-end" of the system, from the occulting mask to the back focal plane, supports experimentation with diverse coronagraph configurations and apodizations. OAP3 re-collimates

*Erkin.Sidick@jpl.nasa.gov; Phone 1 818 393-7585; Fax 1 818 393-3290; www.jpl.nasa.gov

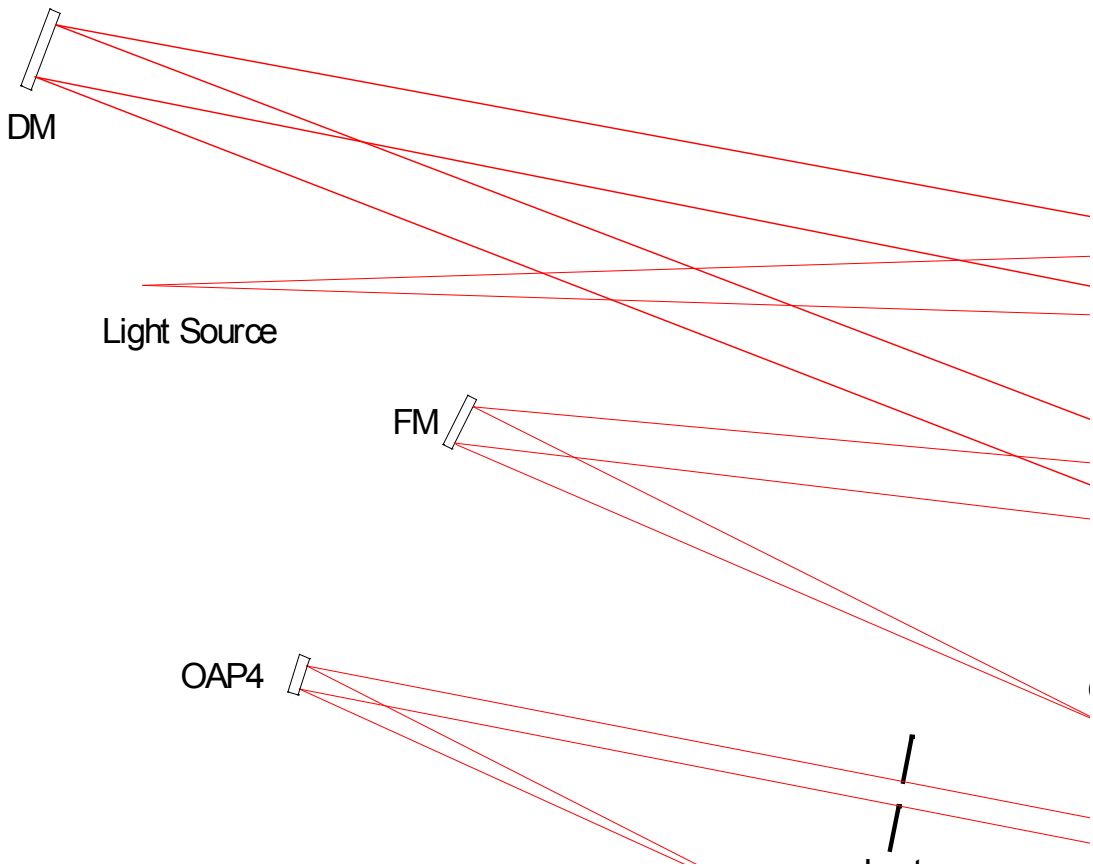

Figure 1. Schematic diagram of the High Contrast Imaging Testbed (HCIT) layout. The light source ("starlight") is a 5μm pinhole illuminated by an optical fiber, and a CCD science camera is located at the back focal plane for detecting the image of the "starlight".

the light passing through the occulter mask and forms a sharp image of the DM pupil at the Lyot plane. A Lyot-stop blocks the ring-likeresidual light diffracted off the occulting mask while letting most of the planet light and aberrated starlight through. After OAP4 forms an image from the remaining stellar and planet lights, it is then magnified ($M \approx 3$) by the OAP5-OAP6 pair for proper sampling on the CCD science camera located at the back focal plane. More information on the HCIT and the DM can be found in Refs. [1-3].

2.2 Optical Components

The DM used on the HCIT has 64x64 actuators arrayed on a 1mm pitch. Its description is similar to the 32x32 actuator DM described in detail in Ref. [1], and will not be repeated here.

Our Lyot-stop is made from a simple blackened piece of sheet metal with a sharp edge. Its opening (Lyot-stop aperture) has an eye-shape defined by two circles that are shifted with respect to each other in the horizontal direction by a distance of ε in units of D. The value of ε needs to be chosen based on the value of the occulting mask width parameter w, and ε=0.36 in this paper.

In the experiment, the phase error at the system exit pupil was flattened by iterative phase estimation and DM adjustments before the data to be shown later were taken. Therefore, in our simulations, we did not include the surface height errors of the six OAP's and the FM. But we included the phase error, the optical density (OD) dispersion and the phase dispersion of the occulter. Details of the occulter used and electric-field conjugation method are described in Ref. [8].

2.3 Definitions of Half Dark-Hole Area and Contrast

For the current optical system with only one DM, we carry out wavefront control (WFC) over a region Ω_c, where Ω_c is either a D-shaped dark-hole region bound by $X \geq X_{\min}$ and $R \leq R_{\max}$, or a rectangular region bound by $[X_{\min}\ X_{\max}\ Y_{\min}\ X_{\max}]$, with $X = x/f$, $Y = y/f$, $R = \sqrt{X^2 + Y^2}$, x and y are the horizontal and the vertical position variables on the corresponding image-plane, and f is the focal length. For the x- and the y-translations of the occulter, we used an Ω_c with $[X_{\min},\ R_{\max}] = [3.5\ 12]\lambda / D$. For the opaque spots on the occulter, we used $[X_{\min},\ R_{\max}] = [3.5\ 11]\lambda / D$. In the investigation on the effect of dark hole size, we used several sizes of rectangular areas to be described later. We evaluate the performance of the HCIT using either the normalized intensity,

$$I_n(x,y) = I(x,y)/I_0, \tag{1}$$

or the contrast,

$$C(x,y) = I_n(x,y)[T_0/T(x,y)] = [I(x,y)/I_0][T_0/T(x,y)], \tag{2}$$

where $I(x,y)$ is the image intensity of the occulted star, and I_0 is the maximum value of the un-occulted star intensity, $T(x,y)$ is the occulter transmittance, and T_0 is the maximum value of the $T(x,y)$. We keep track of the following three contrast quantities in this paper: (i) C_b, the mean contrast inside a "Big" region Ω_b defined by $[X_{\min},\ R_{\max}] = [4\ 10]\lambda / D$ for the occulter translations and $[X_{\min},\ R_{\max}] = [3.5\ 11]\lambda / D$ for the opaque occulter spots. (ii) C_s, the mean contrast inside a "Small" square region Ω_s defined by $[X_{\min}\ X_{\max}\ Y_{\min}\ X_{\max}] = [4\ \ 5\ -0.5\ 0.5]\lambda / D$. (iii) C_m, the "Maximum" contrast value inside the small square region Ω_s. Similarly, we also use I_b, I_s and I_m to denote the big-region mean, the small-region mean, and the small-region maximum of the normalized intensity $I_n(x,y)$ ..

3. WAVEFRONT CONTROL RESULTS

The sensitivity study of coronagraph performance on various system errors, light bandwidth, and control and score dark-hole areas is an on-going process. Some results of this study have been reported before [7], and some will be reported in the future. In this paper, we report our results for three areas: Lateral and longitudinal translation of occulter, an opaque spot on the occulter, and different dark hole sizes. Before we present our measured and simulated results on the above topics, we first provide a comparison between the MACOS and the PROPER simulation tools.

3.1 Comparison of PROPER with MACOS

We have used either MACOS or PROPER [6, 9] in many studies of Lyot and other coronagraphs. In this sub-section, we present a brief comparison of the two approaches when applied to a Lyot coronagraph on the HCIT. Figure 2 shows a comparison of the normalized intensity results obtained with the Lyot-stop taken out, and when the occulter is placed in three different longitudinal locations: $T_z = -0.6$ mm (the occulter is moved away from the DM), 0mm, and 0.6mm relative to design or nominal position. The top-row shows the normalized intensity maps obtained with PROPER, and bottom-row are their x-profiles obtained with both PROPER and MACOS. The two simulation tools use different sampling intervals in the image-plane: 0.15λ/D per pixel in PROPER, and 0.34λ/D per pixel in MACOS. As we can see from Figs. 2(d-e), the results of PROPER and MACOS agree to a few percent over a wide range of intensity and out to at least to 30λ/D. We repeated the above simulations by putting back in the Lyot-stop with $T_z = -0.8$, 0, and 0.8mm, respectively. The results are shown in Figs. 3(a-f). Again, the two approaches agree to several percent over several orders of magnitude of intensity. We believe the small discrepancy between the two methods comes from the fact that, although PROPER does full diffraction analysis between all elements, it does so with an unfolded optical system and does not account for diffraction being off axis. Whereas MACOS simulates the full optical system depicted in Fig. 1. Another factor contributing to the small discrepancy is the difference in the sampling sizes. The courser sampling in MACOS results in some differences in the peaks and the valleys of the PSF cross-sections shown in Figs. 2(d-f) and Figs. 3(d-e). We conclude from these simulations that

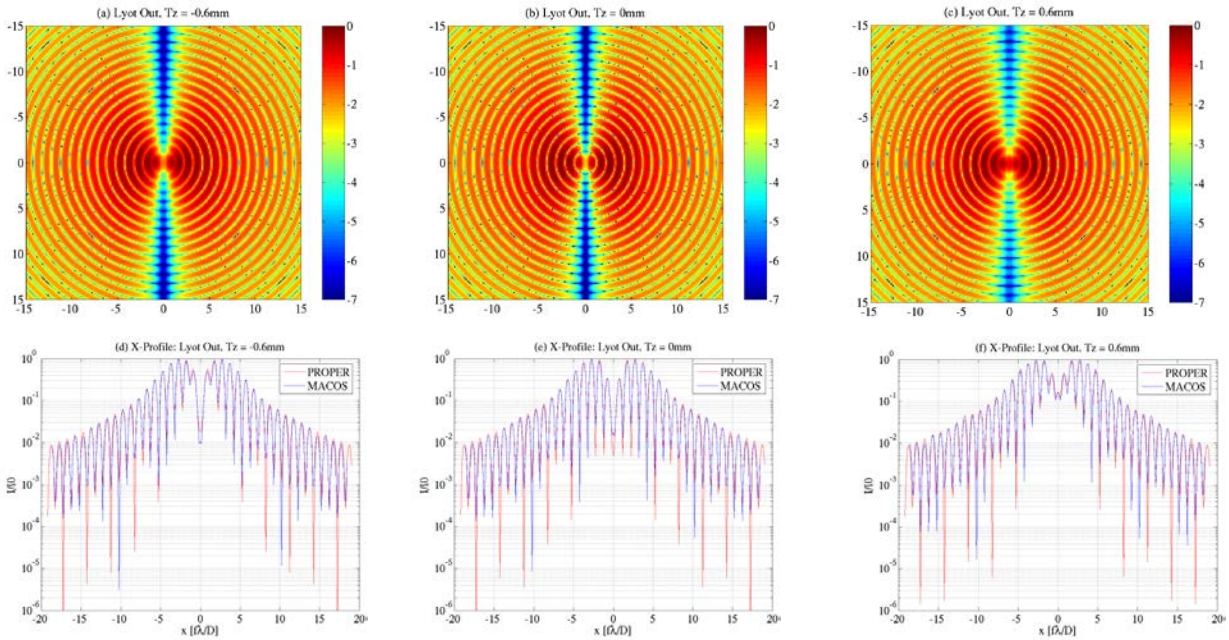

Figure 2. Normalized intensities, $I(x,y)/I_0$, when the Lyot-Stop are taken out. Top-row: $I(x,y)/I_0$ maps obtained using PROPER with the occulter z-translation values of T_z=-0.6mm (occulter is moved away from the DM), 0mm, and 0.6mm (occulter is moved towards the DM), respectively. The units of the x- and the y-axes are λ/D. Bottom-row: The x-cross-section of $I(x,y)/I_0$ maps obtained using PROPER and MACOS with three T_z –values used in the top-row. The sampling is different for PROPER and MACOS.

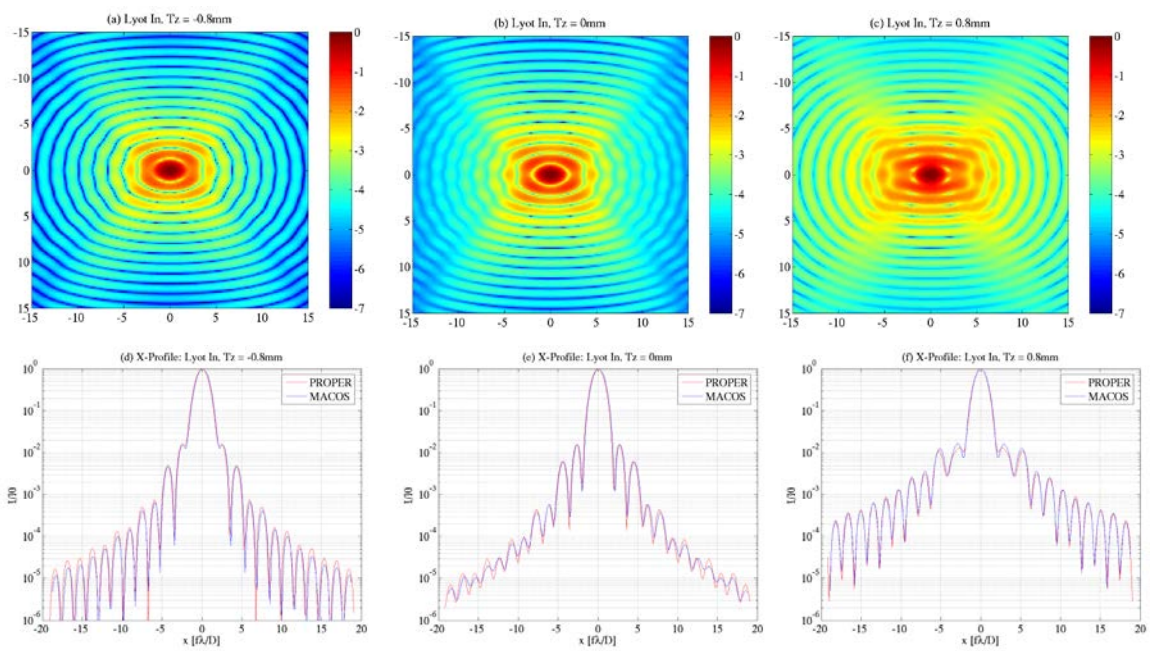

Figure 3. Normalized intensities, $I(x,y)/I_0$, when the Lyot-Stop are put back in. Top-row: $I(x,y)/I_0$ maps obtained using PROPER with the occulter z-translation values of T_z=-0.8mm (occulter is moved away from the DM), 0mm, and 0.8mm (occulter is moved towards the DM), respectively. The units of the x- and the y-axes are λ/D. Bottom-row: The x-cross-section of $I(x,y)/I_0$ maps obtained using PROPER and MACOS with three T_z –values used in the top-row. The sampling is different for PROPER and MACOS.

PROPER and MACOS models are consistent to a few percent over a wide range of intensity and an area that exceeds the dark holes formed in HCIT.

3.2 Longitudinal and Lateral Translation of occulter

The studies whose results will be reported in the next three sub-sections are part of the work of Exoplanet Exploration Coronagraph Technology Milestone Number 3A: Coronagraph starlight suppression: Model validation [10]. The goal of Milestone 3A is to demonstrate the ability to predict the performance sensitivities of a high-contrast imaging system at levels consistent with exoplanet detection requirements. Milestone 3A data was collected in HCIT between January and March, 2013, beginning with longitudinal and lateral occulter translation tests. We denote the amounts of these two types of translation by T_z and T_x, respectively. The experiment and the corresponding simulations of this part were carried out in the following steps:

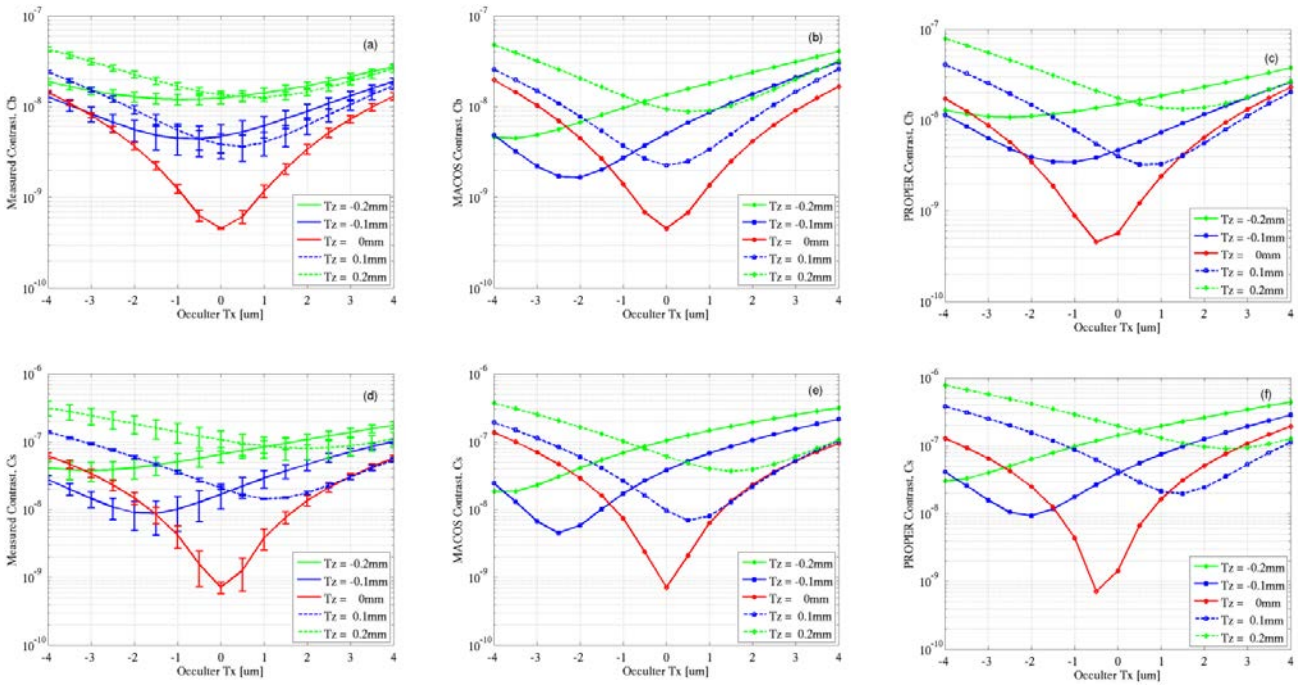

Figure 4. Contrast as a function of occulter lateral translation, T_x, and with longitudinal translation, T_z, as a parameter. The T_x and T_z are defined in the local coordinates of the occulter with T_z parallel to the direction of the chief-ray. (a) Three-day average of the measured C_b. The error bars correspond to the standard deviation (STD) of the three sets data. (b-c) C_b calculated using MACOS and PROPER, respectively. Parts (d-f) are the same as parts (a-c) and show the values of C_s (small box) in place of C_b.

1. Before conducting wavefront control, an occulter T_z-scan was carried out to determine $T_z = T_{z0}$ where the peak intensity at the final focal plane becomes minimum. We found T_{z0} = 0.8mm, where positive T_z (or T_{z0}) moves the occulter towards the DM. This shift is caused by the phase transmission profile of the variable thickness nickel on the mask, and is predicted by models to be also ~0.8 microns.

2. Carried-out 2% narrow-band wavefront control with the occulter positioned at this new location, T_{z0} = 0.8mm and set to the DM to form a dark-hole. For simulations, we tried both monochromatic and 2% narrow-band beams, and got very similar results. For the translation tests, we present the results obtained with the monochromatic model only.

3. Because the mechanical translation axis was not necessarily aligned to the optical axis, we had to determine a lateral zero point for each axial position. We did this by first setting the DM actuators to the heights obtained in Step 2, removing the Lyot-Stop, then moving the occulter longitudinally to a new position $T_z' = T_z + T_{z0}$ before carrying out an occulter T_x–scan. We then determined the value of $T_x = T_{x0}$ at which the intensities of the first

Airy-ring side-lobes on either side of the center of the image were equal. This step was repeated for five values of T_z, that is, T_z = -0.2, -0.1, 0, 0.1 and 0.2mm.

4. We then reinstalled the Lyot Stop and scanned te occulter in x for each T_z-value, that is, the occulter was translated laterally by $T_x' = T_x + T_{x0}$, and we recorded the values of C_b and C_s. We repeated this step for all five values of T_z.

The same procedure was followed in the simulations. We did not keep track of the T_{x0}–values obtained in the experiment, and they may be different from what we got in the simulations.

In Figs. 4(a-f), we plot C_b and C_s as a function of T_x with T_z as a parameter. As expected, simulation yields contrast values better than the measured ones because the simulations do not account for any experimental floor (e.g. incoherent scattered light). Therefore, for the purpose of comparison, we set as the minimum for all model curves the contrast at $T_x = T_z = 0$ and added this value to all the simulated data.

Figures 5(a-d) show the percentage errors between the measured and the calculated C_b and C_s values, where the error is defined as (Calculated – Measured) / Calculated (including the contrast floor). The predicted C_b and C_s curves exhibit similar behaviors as those of the measured ones, but the valleys of the $T_z \neq 0$ curves take place at T_x-values slightly different than those of the measured ones. Overall, the results of PROPER agree with the measurement better than those of MACOS. Also, most predicted data points differ from the measurements with a factor of 2. The exact reasons that cause the difference observed between the prediction and the measurement for these tests is still under investigation.

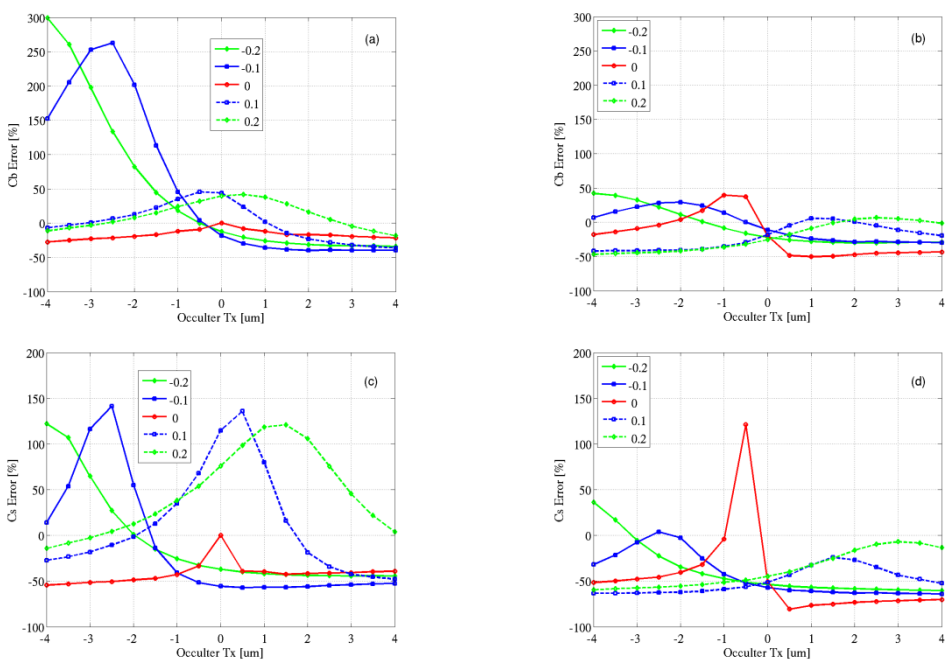

Figure 5. Percentage contrast error, defined as 100×(Calculated – Measured) / Calculated, as a function of occulter lateral translation, T_x, with longitudinal translation, T_z, as a parameter. (a) C_b error: MACOS versus measured. (b) C_b error: PROPER versus measured. (c) C_s error: MACOS versus measured. (d) C_s error: PROPER versus measured. Shown on the figure legends are T_z-values in mm.

The dependence of contrast leakage in the dark hole is approximately quadratic in the lateral translation parameter. If we fit a second-order polynomial to the curves in Figs. 4(a-c) in the form of

$$C_b = a(T_z)[T_x - x_0(T_z)]^2 + b(T_z), \qquad (1)$$

we obtain the fitting parameter values listed in Table 1. The values of $a(T_z)$, $x_0(T_z)$ and $b(T_z)$ are plotted as a function of T_z in Figs. 6(a-c) respectively. These data are useful in predicting the sensitivity of a Lyot coronagraph's narrow-band contrast to the occulter position.

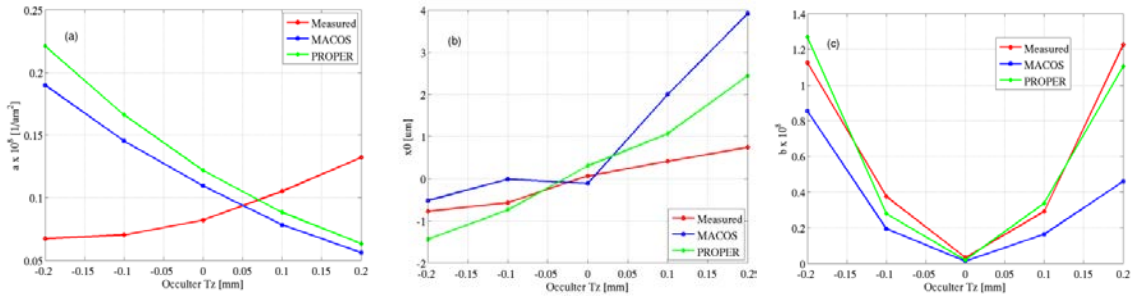

Figure 6. Fitting parameters defined in Eqn. (1) and listed in Table 1.

Table 1. Values of the fitting parameters defined in Eqn. (1).

	Measured			MACOS			PROPER		
Tz [mm]	$ax10^8$ [1/um^2]	x_0 [um]	$bx10^8$	$ax10^8$ [1/um^2]	x_0 [um]	$bx10^8$	$ax10^8$ [1/um^2]	x_0 [um]	$bx10^8$
-0.2	0.0672	-0.7733	1.1261	0.1900	-0.5199	0.8539	0.2210	-1.4394	1.2688
-0.1	0.0702	-0.5677	0.3757	0.1453	-0.0119	0.1939	0.1661	-0.7386	0.2789
0	0.0821	0.0641	0.0328	0.1094	-0.1123	0.0133	0.1217	0.3032	0.0187
0.1	0.1052	0.4132	0.2915	0.0784	1.9982	0.1638	0.0882	1.0678	0.3374
0.2	0.1322	0.7453	1.2267	0.0561	3.9111	0.4600	0.0634	2.4388	1.1043

3.3 Opaque Spot on the occulter Surface

The next topic of our report is the effect of an opaque spot on 10% broadband contrast. In order to evaluate the effect of small extraneous inclusions such as a dust particle or a coating defect on the performance of the occulter, we added a few marks at chosen locations on the mask. The occulting mask was originally fabricated by a vacuum deposition process for the TDEM Milestone 2 demonstration [11]. This is a linear mask, i.e., the mask profile is along one dimension with the other dimension ideally constant. The mask profile is described elsewhere [8] and is made with varying thickness of a nickel layer to obtain the required transmission profile. We added square shaped marks of platinum on this mask at chosen locations as shown in Fig. 7. Figure 8(a) shows one of the marks under SEM. The rectangular shape under SEM is due to the 52 deg tilted observation of square mark. The debris field seen was present on the mask before the marks were written by focused ion beam (FIB) technique. A dual beam SEM/FIB system (NOVA 600-D24 from FEI Company) at Caltech was employed for writing these Pt marks of required thickness and area. Mark C3 shown on Fig. 8(b) is about 170nm tall with optical density ~8. Similarly, the mark C4 in Fig. 8(c) is about 150nm

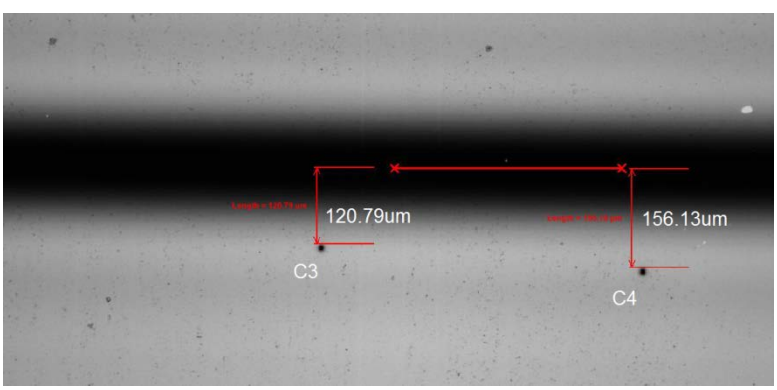

Figure 7. AFM image of the C3- and the C4-spot areas on the occulting mask.

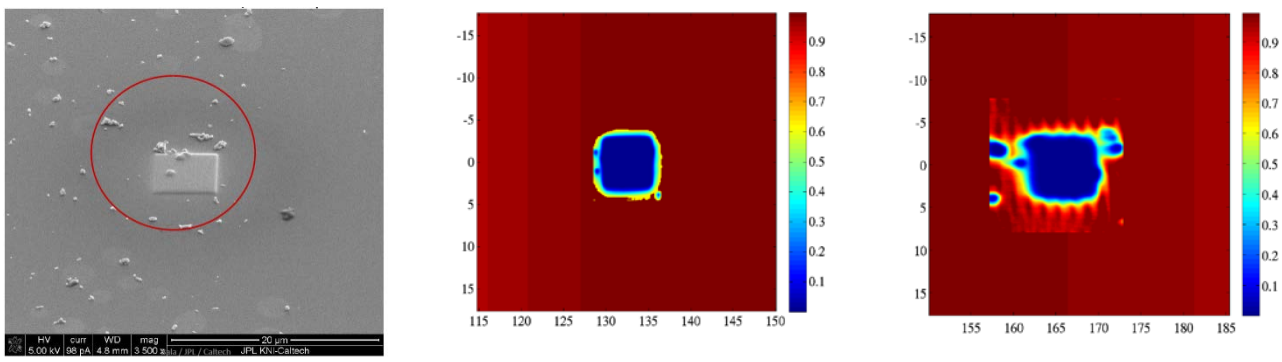

Figure 8. (a) AFM image of the C3-spot area on the occulting mask. (b) Measured C3-spot transmission map superimposed into the occulter transmission model. The pixel size is 0.0984μm. (c) Measured C4-spot transmission map superimposed into the occulter transmission model. The pixel size is 0.1228μm. These two occulter transmission maps are re-sampled to a pixel size of 8.492μm in MACOS model. In parts (b) and (c), the horizontal and the vertical axis labels are positions in μm.

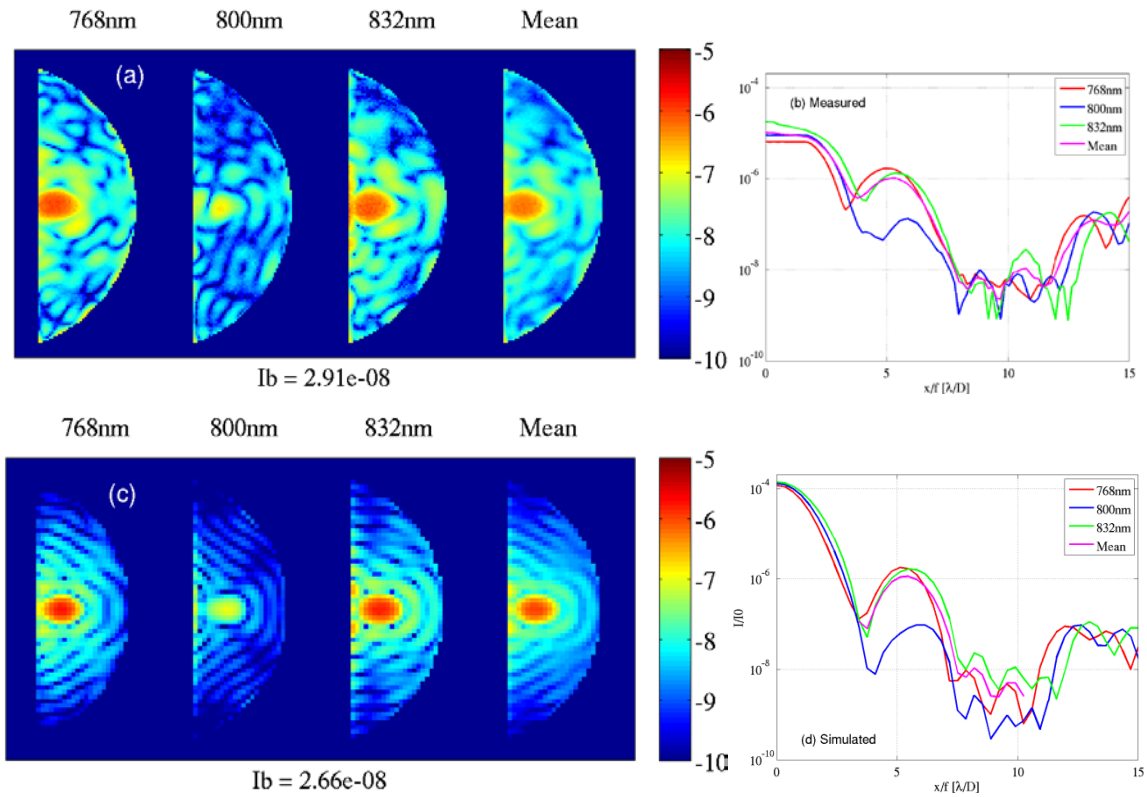

Figure 9. Log-scale normalized intensity, $I_n(x,y)$, maps obtained with the C3-spot occulter area. The top row shows the measured data, and the bottom row shows the corresponding simulated results. The first three maps in parts (a) and (c) correspond to three different 2%-filters, and the fourth parts are their mean values or 8%-broadband $I_n(x,y)$ maps. Parts (b) and (d) show the x-cross sections of the four corresponding $I_n(x,y)$ maps. The I_b –values listed in the bottoms of parts (a) and (c) are the broadband normalized intensities.

tall with optical density ~6. These marks are about 6um squares as measured by AFM and SEM. Two dimensional optical transmission profiles of these marks were calculated based on 2-D maps of the marks from AFM and using known optical constants of Pt. Figure 8(b) shows the part of the occulter transmission coefficient (amplitude) map on which the fine-sampled C3-spot is superimposed, and Fig. 8(c) shows the same for C4-spot. After an opaque spot is added to the occulter transmission amplitude in this way, the occulter map is down-sampled to its normal MACOS pixel-size of 8.492μm, and wavefront control simulation is carried out with this modified occulting mask.

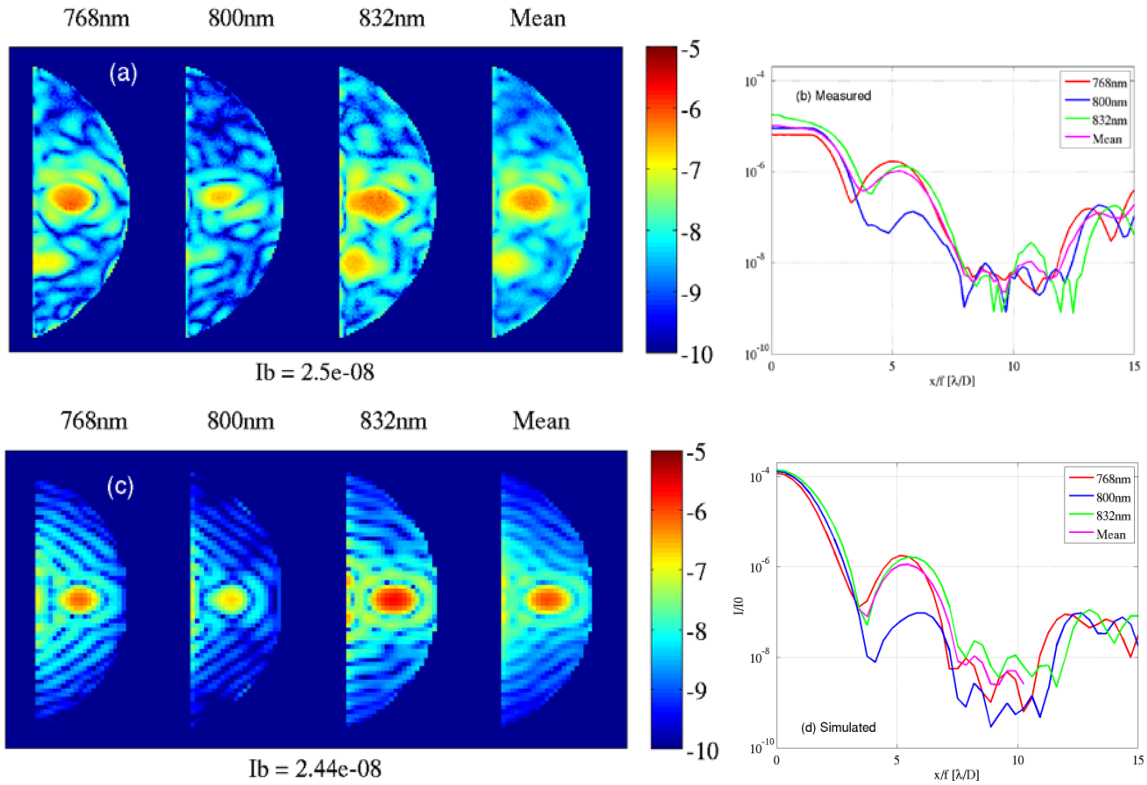

Figure 10. Same as Fig. (9) for the C4-spot area of the occulter.

Table 2. Measured and predicted 2% and 8% (Mean) normalized intensities, or I_b-values, and the measured-to-predicted ratios obtained from the C3- and C4-post areas of the occulter. The simulated results were obtained assuming monochromatic beam.

Box Size	Spot Name	Contrast Type	768nm	800nm	832nm	Mean
Dark-Hole Area	C3-Spot	Measured, x10^{-8}	4.17	0.61	3.96	2.91
		Simulated, x10^{-8}	3.55	0.27	4.17	2.66
		Ratio: Meas/Simul	1.17	2.25	0.95	1.09
	C4-Spot	Measured, x10^{-8}	2.81	0.92	3.78	2.50
		Simulated, x10^{-8}	1.57	0.48	5.28	2.44
		Ratio: Meas/Simul	1.79	1.91	0.72	1.03
2λ/D-Wide Spot Area	C3-Spot	Measured, x10^{-6}	1.49	0.08	1.06	0.88
		Simulated, x10^{-6}	0.86	0.05	0.89	0.60
		Ratio: Meas/Simul	1.73	1.67	1.19	1.46
	C4-Spot	Measured, x10^{-6}	0.91	0.16	0.93	0.67
		Simulated, x10^{-6}	0.34	0.09	1.10	0.51
		Ratio: Meas/Simul	2.69	1.82	0.85	1.31

Figures 9(a-d) compare the predicted maps of the normalized intensity with the measured ones for the C3 occulter spot, and Figs. 10(a-d) show the same results for C4 occulter spot. Among them, part (a) shows the measured individual and the averaged intensity maps, and part (b) shows their x-profiles at $Y = 0$. Parts (c-d) show the corresponding simulated results. The measurements and the predictions come close in this case, especially the broadband I_b–values listed in the bottom of each intensity map plot. The residual Airy-rings are visible in the predicted maps, but they were washed out in the measured ones. One reason causing such a difference is that some residual exit-pupil phase error still exists in the experiment, but it was not included in the simulation. The measured normalized intensities in Fig. 10(a) display an evidence of the second occulting defect near C4-spot. That spot was not intentional and was not included in our

simulations In Table 2, we listed the I_b–values of the measured and the simulated normalized intensities at three individual wavelengths as well as their average values. As we can see from this table, the agreement between the measurement and the prediction is typically between a factor of 0.7 and 2.

3.4 Different Dark-Hole Sizes

The last topic that we are going to cover is the dependency of the broadband control efficiency on the dark-hole size. In theory, a 48x48 actuators DM can control a region up to $R_{max} = 24\lambda/D$ when the exit-pupil covers the whole diameter of the DM. In order to understand the dependency of broadband wavefront control efficiency on the dark-hole region, we carried out control experiments and simulations for three dark-hole sizes with $[X_{min}, R_{max}]$ = [3.5 15] and [3.5 20]λ/D in the first two cases and with $[X_{min}, X_{max}, Y_{min}, Y_{max}]$ = [3.5, 24, -10, 10]λ/D in the last one. The experiments were carried out in the 768, 800, and 832 nm filters, with the resulting images combined to form a composite broad-band image. The I_b and I_s results of all four cases are summarized in Table 3, and the measured and the simulated $I_n(x,y)$ maps of the three cases with increased dark-hole sizes are shown in Fig. 11. The data includes several defects that correspond to particulate contamination of the mask, especially near the lower right side of the dark hole. The data show that indeed we could control the dark hole out to the theoretical limit of the DM with a factor of 3 loss of contrast (vs. a predicted factor of two loss from the simulation) at the inner working angle (the I_s box). The predicted contrast within the I_s box was within a factor of 2 of the measured contrast for the 15 λ/D and 20 λ/D cases, while it was off by a factor of 2.3 for the 24 λ/D case. We also observed that the average contrast in the full dark hole *improved* as the dark hole grew larger. We believe this is because the Airy rings are less pronounced at larger radii, so the DM does not have to work as hard to achieve high contrast at these angles. However, the simulation did not bear this out and predicted a slight increase (from 4.9e-11 to 6.9e-11) in overall contrast. In the above simulations, we included the phase-error estimated at the exit-pupil of the current optical system. When that phase-error was not included, our simulation yielded $I_b = 4.75\times10^{-11}$, 4.41×10^{-11} and 5.57×10^{-11} for the three different dark-hole sizes, respectively. That is, the exit-pupil phase-error did not introduce any meaningful change to the simulated final big-box mean contrast values.

Table 3. Broadband I_b-values corresponding to four different dark-hole sizes. The experiments were carried out with three 2%-bandpass filters centered at 768, 800 and 832nm, but those three beams were modeled as monochromatic beams in simulations. The dark-hole size parameters are $[X_{min}, R_{max}]$ in the first three cases, and $[X_{min}, X_{max}]$ in the last one.

Dark-Hole Size		3.5 to 15λ/D	3.5 to 20λ/D	3.5 to 24λ/D
I_b	Measured	$1.32\text{x}10^{-9}$	$1.02\text{x}10^{-9}$	$9.91\text{x}10^{-10}$
	Simulated	$4.91\text{x}10^{-11}$	$5.59\text{x}10^{-11}$	$6.90\text{x}10^{-11}$
I_s	Measured	$1.61\text{x}10^{-9}$	$2.37\text{x}10^{-9}$	$4.36\text{x}10^{-9}$
	Simulated	$9.93\text{x}10^{-10}$	$1.71\text{x}10^{-9}$	$1.87\text{x}10^{-9}$

4. CONCLUSION

We have shown that our models are predicting contrast sensitivity to within a factor of 2 for contrast levels in the 1e-9 to 1e-8 region, for mask motion, mask defects, and contrast at the IWA for different dark hole sizes. We have formed dark holes out to the theoretical limit of our 48x48 illuminated deformable mirrors.

Our work suggests that in predicting coronagraph contrast performance, e.g. sensitivity-based predictions such as Ref. 12, a factor of 2 should be carried for the model uncertainty factor. In future work we will report on model and data agreement for different wavelength control bandwidths, non-functional DM actuators, and the ability to discriminate instrument-induced speckles from other background sources. These experimental validations of key coronagraph sensitivity factors will additionally contribute to the confidence in performance prediction models for future flight systems.

This work was carried out at the Jet Propulsion Laboratory, California Institute of Technology, under contract with the National Aeronautics and Space Administration. Funding was provided through the 2010 Technology Demonstrations for Exoplanet Missions (TDEM) Strategic Astrophysics Technology proposal.

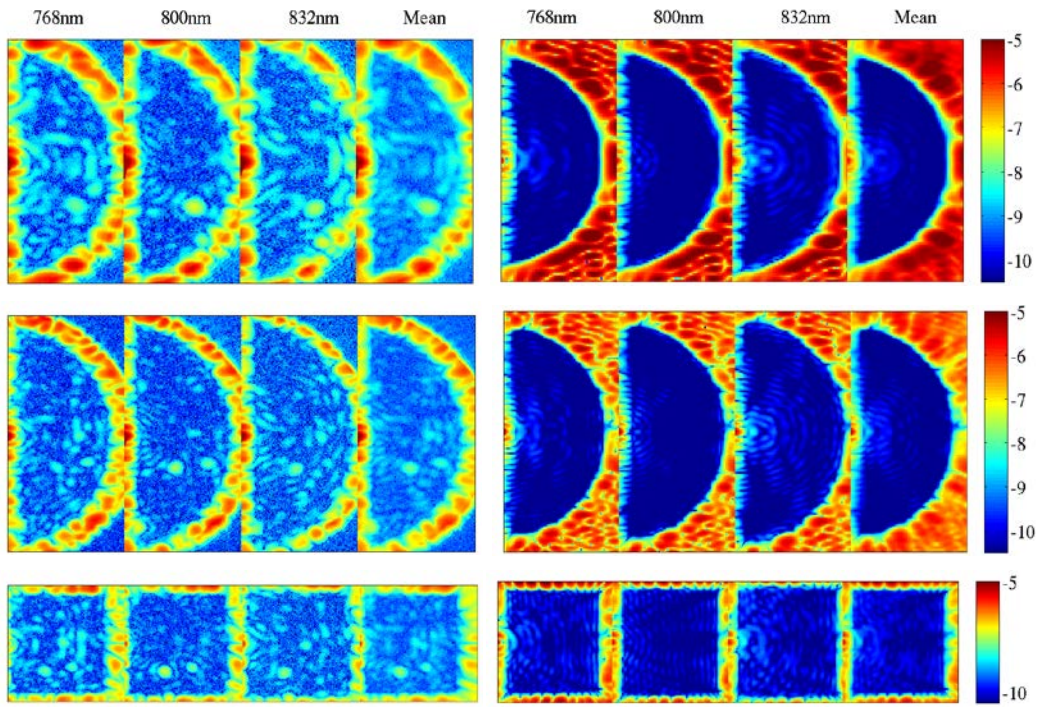

Figure 11. Left-column: Measured $I_n(x,y)$ maps at three 2%-bands and their mean corresponding to two D-shaped dark-hole areas with $[X_{min}, R_{max}]$ = [3.5 15], and [3.5 20]λ/D, and one rectangular area with $[X_{min}, X_{max}, Y_{min}, Y_{max}]$ = [3.5, 24, -10, 10]λ/D. Right-column: The corresponding simulated $I_n(x,y)$ maps obtained with monochromatic beams. The corresponding I_b and I_s values are listed in Table 3. (ERKIN, SHOW THESE AT THE SAME SPATIAL SCALE. THAT WAY THE IMMENSE SIZE Of the 24 L/D DARK HOLE WILL BE IMPRESSIVE.

REFERENCES

1. John T. Trauger, Chris Burrows, Brian Gordon, Joseph J. Green, Andrew E. Lowman, Dwight Moody, Albert F. Niessner, Fang Shi, and Daniel Wilson, "Coronagraph contrast demonstrations with the high-contrast imaging testbed," *Proc. SPIE*, **5487**, 1330 (2004).
2. Andrew E. Lowman, John T. Trauger, Brian Gordon, Joseph J. Green, Dwight Moody, Albert F. Niessner, and Fang Shi, "High-contrast imaging testbed for the Terrestrial Planet Finder coronagraph," *Proc. SPIE*, **5487**, 1246 (2004).
3. Erkin Sidick, Fang Shi, Scott Basinger, Dwight Moody, Andrew E. Lowman, Andreas C. Kuhnert, and John T. Trauger, "Performance of TPF's High-Contrast Imaging Testbed: Modeling and simulations, " *Proc. SPIE*, **6265**, 62653L (2006).
4. Amir Give'on *et al*, "Broadband wavefront correction algorithm for high-contrast imaging system," *Proc. SPIE*, **6691**, 66910A (2007).
5. *Modeling and Analysis for Controlled Optical Systems User's Manual*, Jet Propulsion Laboratory, California Institute of Technology, Pasadena, CA.
6. John E. Krist, "PROPER: an optical propagation library for IDL," *Proc. SPIE*, **6675**, 66750P-1 (2007).
7. Erkin Sidick, Stuart Shaklan, Amir Give'on, and Brian Kern, " Studies of the effects of optical system errors on the HCIT contrast performance," *Proc. SPIE*, **8151**, 8151-06 (2011).
8. Erkin Sidick, Stuart Shaklan, Kunjithapatham Balasubramanian, "HCIT Broadband Contrast Performance Sensitivity Studies", *Proc. SPIE*, 8520, 85200M-1 (2012).
9. John E. Krist, Ruslan Belikov, Laurent Pueyo, Dimitri P. Mawet, Dwight Moody, John T. Trauger, Stuart B. Shaklan, "Assessing the performance limits of internal coronagraphs through end-to-end modeling: a NASA TDEM study," *Proc. SPIE*, **8151**, 81510E-1 (2011).

10. "Exoplanet Exploration Coronagraph Technology: Technology Milestone #3 White Paper," Stuart Shaklan editor, 5 Jan. 2009, http://exep.jpl.nasa.gov/files/exep/ExEPC%20Milestone%203%20white%20paper%20signed.pdf.
11. "Exoplanet Exploration Coronagraph Technology: Technology Milestone #2 Report," Brian Kern, Andreas Kuhnert and John Trauger, editors, 8 Aug. 2008, http://exep.jpl.nasa.gov/TPF-C/HCIT-Milestone2Signed-2008-08-08.pdf.
12. S. Shaklan, L. Marchen, J. Krist, and M. Rud, "Stability error budget for an aggressive coronagraph on a 3.8 m Telescope," *Proc. SPIE*, **8151**, 815109-1 (2011).